Petroleum Science 23 (2026) 4855–4872

Contents lists available at ScienceDirect

Petroleum Science

journal homepage: www.keaipublishing.com/en/journals/petroleum-science

Original Paper

Study on gas–liquid counter-current flow behavior and calculation of key killing parameters using bullheading well control method in directional wells

Bang-Tang Yin [a,b,*], Tian-Bao Ding [a,b], Wei Zhang [c], Shu-Long Wang [a,b], Zhi-Yuan Wang [a,b], Bao-Jiang Sun [a,b], Xu-Liang Zhang [c], Qian-Li Ma [d]

[a] *National Key Laboratory of Deep Oil and Gas, China University of Petroleum (East China), Qingdao, 266580, Shandong, China*
[b] *School of Petroleum Engineering in China University of Petroleum (East China), Qingdao, 266580, Shandong, China*
[c] *PetroChina Tarim Oilfield Company, Korla, 841000, Xinjiang, China*
[d] *CNPC Great Wall Drilling Company Limited, Beijing, 100101, China*

A R T I C L E I N F O

Article history:
Received 23 January 2025
Received in revised form
24 December 2025
Accepted 31 March 2026
Available online 4 April 2026

Edited by Jia-Jia Fei

Keywords:
Deep reservoirs
Directional wells
Bullheading well control
Gas–liquid counter-current flow
Well control parameters
Flow pattern transition

A B S T R A C T

The formation pressure system of deep and ultra-deep carbonate reservoirs is complex, with widespread fracture development and a narrow safety pressure window. The use of conventional cyclic well control methods often leads to overpressure and leakage alternation. The bullheading well control method is a commonly used technique to address blowouts in such oil and gas reservoirs. However, during the bullheading method, gas–liquid counter-current two-phase flow is frequently encountered, yet it remains inadequately studied. This gap in scientific understanding may result in potential hazards. This study carried out experiments to investigate gas–liquid counter-current two-phase flow at various inclination angles and viscosities. The research revealed the transition behaviors of the flow and developed a set of criteria to identify shifts in the flow patterns. A model for two-phase flow in bullheading well control within the wellbore was developed. The discrepancy between the predicted and observed casing pressures during the well control phase was found to be within 15%. In addition, the study explored the effects of flow rate, density, and viscosity of the well control fluid on wellbore pressure and the distribution of gas holdup. The results indicate that a higher fluid flow rate leads to a shorter well control duration but causes an increase in casing pressure at the wellhead. On the other hand, an increase in fluid density accelerates the reduction in casing pressure, ultimately lowering the pressure at the wellhead. Increasing the viscosity of the well control fluid slows down the casing pressure decline, leading to a higher wellhead casing pressure, while the required backflow time decreases. The research suggests that appropriately increasing the density and viscosity of the well control fluid can improve the efficiency of bullheading operations for well control.

1. Introduction

Exploration efforts are increasingly shifting from easily accessible areas to more challenging regions with harsh environmental conditions and higher extraction difficulties these years (Mu et al., 2020). Among them, carbonate reservoirs are crucial to global petroleum resources (Burchette, 2012). These reservoirs are typically located at greater depths and are associated with intricate geological settings. They also pose several challenges, including restricted safety pressure margins, considerable variability, and the presence of well-developed natural fractures (Pal et al., 2018; Tan et al., 2022), all of which add complexity to their management. These characteristics make it difficult to effectively manage overflow incidents, where conventional cyclic well control methods may not suffice. The bullheading well control method, an important well control technique, has been widely used in deep carbonate reservoirs of Tarim Basin. This method involves pumping well control fluids into the wellbore from the surface after detecting an overflow, directly pushing the intruding fluid back

* Corresponding author.
E-mail address: yinbangtang@163.com (B.-T. Yin).
Peer review under the responsibility of China University of Petroleum (Beijing).

https://doi.org/10.1016/j.petsci.2026.03.067
1995-8226/

into the formation, thereby restoring pressure balance within the wellbore. This non-traditional well control approach is alternatively referred to as the hard-top method or the direct-push technique.

Oudenman and his co-workers (Oudeman, 1999; Oudeman et al., 1994) conducted theoretical studies and field verification of the bullheading method, though it is only applicable when the wellbore is entirely filled with static gas. Flores-Avila et al. (2002, 2003) developed a bullheading well control model based on the assumption that gas well blowouts are equivalent to gas production, using IPR and well control curves. Teng et al. (2018) introduced a bullheading well control approach consisting of five steps and outlined methods for calculating the relevant parameters. Zhou et al. (2021) accounted for the influence of fluid displacement, developing models for the bullheading process in wells that are primarily liquid or primarily gas, and analyzed the wellbore pressure variation. Wang et al. (2025) developed a transient model for bullheading and examined how well killing parameters are affected. The research mentioned above is based on the theory of co-current gas–liquid flow within the wellbore.

During the bullheading operation, gas ascends while the well control fluid descends, resulting in a counter-current two-phase flow composed of both gas and liquid. This interaction between the two phases makes their distribution within the pipeline more complex. Different phase distributions can transition into various flow regimes, leading to more complex flow behaviors. Taitel and Barnea (1983) were among the first to study the behavior of gas–liquid counter-current flow in vertical pipes. They developed criteria that define the transition between various flow regimes, such as the shift from bubble flow to slug flow and from slug flow to annular flow. Similarly, Yamaguchi and Yamazaki (1982, 1984) conducted experimental research on gas–liquid counter-current flow under standard ambient conditions, categorizing the observed flow patterns into bubble flow, slug flow, and annular flow, while also introducing methods for predicting gas holdup. Hasan et al. (1994) concentrated on establishing transition criteria for the change from bubble flow to slug flow and created a model to estimate gas holdup, based on experiments using air and water at standard conditions. Kim et al. (2001) investigated the transition thresholds between slug flow and annular flow in air-water systems, particularly at ambient temperature and pressure. Ghosh et al. (2012) extended their experimental studies to encompass a wider range of apparent gas–liquid velocities, identifying slug and annular flow as prevailing flow pattern. Lastly, Besagni and Inzoli (2016) employed image analysis to explore the effects of gas–liquid counter-current flow on bubble shape, size, and distribution, finding that reverse flow notably increases gas holdup and decreases the velocity of bubble rise. Sukamta et al. (2018) investigated slug flow behavior in small-diameter vertical pipes, finding that increased gas–phase velocity caused the flow pattern to shift towards slug flow and mist flow, while increased liquid-phase velocity led to bubble flow. Liu et al. (2023) conducted experimental investigations on gas–liquid two-phase counter-current flow within vertical pipes. In a similar study, Ren et al. (2024) examined the impact of wellbore inclination, liquid viscosity, gas–liquid velocity, and bubble size on bubble migration during reverse flow. Their results indicated that an increase in wellbore inclination, liquid viscosity, and the opposing velocity of the liquid flow relative to the bubble flow led to a gradual reduction in the migration velocity of Taylor bubbles. This effect led to a reduction in the upward movement of larger bubbles.

Currently, most studies on the transitions between gas–liquid two-phase flow regimes focus predominantly on co-current flow configurations. In contrast, investigations into the behavior of gas–liquid counter-current flow remain relatively scarce, particularly under conditions of inclined pipes and high-viscosity liquid phases. In complex geological environments, existing models cannot accurately predict the distribution and transition of gas–liquid counter-current flow regimes during bullheading well control in directional wells, warranting further investigation. Additionally, the application of the bullheading method requires careful consideration of formation conditions, intruding fluid properties, and wellhead pressure-bearing capacity. It is crucial to ensure safety while minimizing damage to the reservoir, as improper use may lead to catastrophic blowout incidents. Therefore, determining key parameters for bullheading well control is critical.

In conclusion, the bullheading well killing method holds significant potential in complex geological conditions and special operational scenarios. Existing models fail to adequately consider factors such as the properties of the liquid phase, wellbore inclination, and gas content, leading to an incomplete understanding of bubble migration and the transition of flow patterns in gas–liquid counter-current flow. To address these limitations, the present study conducts experiments on gas–liquid counter-current two-phase flow, revealing transition behaviors and establishing pertinent criteria. Based on the bubble migration velocity model, a gas–liquid two-phase flow model for bullheading well control is subsequently developed, accompanied by calculation methods for well control parameters. The study further analyzes field data to assess the influence of well control fluid density, viscosity and flow rate on wellhead pressure, casing shoe pressure, and gas holdup distribution. It also proposes a calculation method for determining bullheading well control parameters, offering theoretical insights for field applications.

2. Gas–liquid counter-current flow behavior

2.1. Gas–liquid counter-current pattern distribution and transition characteristics

2.1.1. Gas–liquid counter-current pattern distribution

In order to examine the transition behaviors of flow patterns in gas–liquid counter-current two-phase flow, experiments were conducted with varying wellbore inclination angles and liquid phase viscosities. A detailed account of the experimental setup and conditions is provided in reference (Ren et al., 2024), as illustrated in Fig. 1. The main experimental parameters are outlined in Table 1.

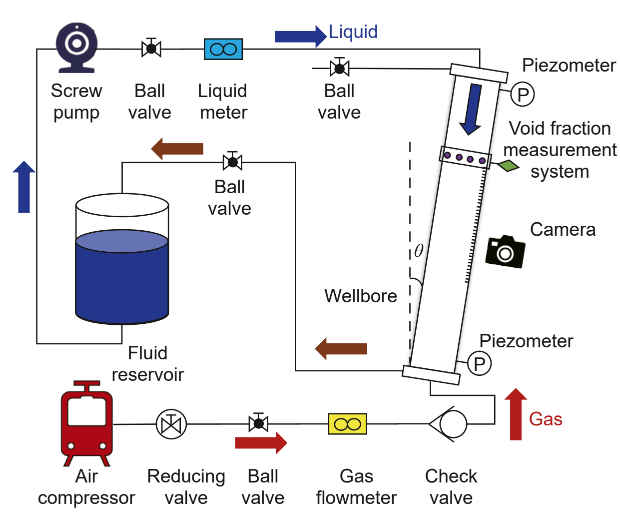

Fig. 1. Experimental schematic diagram (Ren et al., 2024).

Table 1
The basic experimental parameters.

Parameters	Value
Experimental fluid	Air, deionized water and carboxymethyl cellulose (CMC) solution
Viscosity of gas	0.0176 mPa·s
Viscosity of liquid	1, 15, 35 and 50 mPa·s
Angle of inclination	0°, 10°, 20°, 30°, 40°, 50° and 60°
Gas velocity	0.004, 0.008, 0.012, 0.02 and 0.05 m·s^{-1}
Liquid velocity	0.03, 0.04, 0.08, 0.12 and 0.2 m·s^{-1}
Gas density	1.2 kg·m^{-3}
Liquid density	1000 kg·m^{-3}

The flow patterns observed during gas–liquid counter-current flow resemble those found in co-current gas–liquid flow. However, notable differences were found in the distribution and movement characteristics of bubbles within the wellbore when compared to co-current flow. The bubble migration behavior in gas–liquid counter-current two-phase flow was extensively analyzed in our prior study (Ren et al., 2024). According to the bubble morphology and gas–liquid flow characteristics in the wellbore, different flow patterns were divided. Throughout the experiment, the flow patterns within the wellbore consisted of bubble flow, cap-bubble flow, slug flow, and annular flow, with no occurrence of churn flow, as depicted in Fig. 2.

2.1.2. Gas–liquid counter-current pattern transition characteristics

Under gas–liquid counter-current flow conditions, the bubble flow behavior deviates from that in co-current flow, driven by variations in both the superficial gas and liquid velocities. These differences manifest in the following ways:

(1) Under the condition of a constant liquid-phase superficial velocity, increasing the gas-phase superficial velocity leads to a transition in flow pattern from bubble flow to churn flow and slug flow (Ghiaasiaan et al., 1995), as shown in Fig. 3. The reasons for this change can be attributed to two factors: First, as the gas-phase superficial velocity increases, the number of bubbles in the wellbore rises, enhancing the probability of small bubbles colliding and coalescing into larger ones. Simultaneously, the increase in bubble rise velocity intensifies the wake effect, further promoting collision and coalescence among bubbles.

(2) When the superficial liquid velocity is raised while maintaining a constant gas superficial velocity, the drag force on the bubbles increases, which reduces their upward velocity as the liquid flow rate rises. However, due to the stronger tailing effect, the frequency of bubble oscillations grows, leading to a higher likelihood of bubble collisions and coalescence, as illustrated in Fig. 4. As the average bubble size increases, the flow pattern shifts from bubble flow to either cap-bubble or slug flow.

2.2. Gas–liquid counter-current two-phase flow pattern transition criterion

2.2.1. Bubble flow to cap-bubble flow transition

Currently, studies on co-current gas–liquid flow often overlook the intermediate flow patterns during the bubble-to-slug transition. In this experiment, cap-bubble flow was observed under counter-current gas–liquid two-phase flow conditions, thus enriching the flow pattern map for counter-current gas–liquid flow. Experimental findings from this study indicate that the critical gas volume fraction necessary for this transition is approximately 0.15.

In the realm of gas–liquid co-current two-phase flow, the gas volume fraction within a pipe is defined as the ratio of the apparent velocity of the gas phase to its actual upward velocity. Research conducted by scholars (Taitel and Barnea, 1983; Ghiaasiaan et al., 1995, 1997; Yamaguchi and Yamazaki, 1982, 1984) has demonstrated that the distribution of gas volume fraction in a pipe can be effectively correlated with theories developed for co-current gas–liquid flows, even when applied to gas–liquid counter-current flow conditions. These researchers have significantly contributed to the formulation of a calculation model for

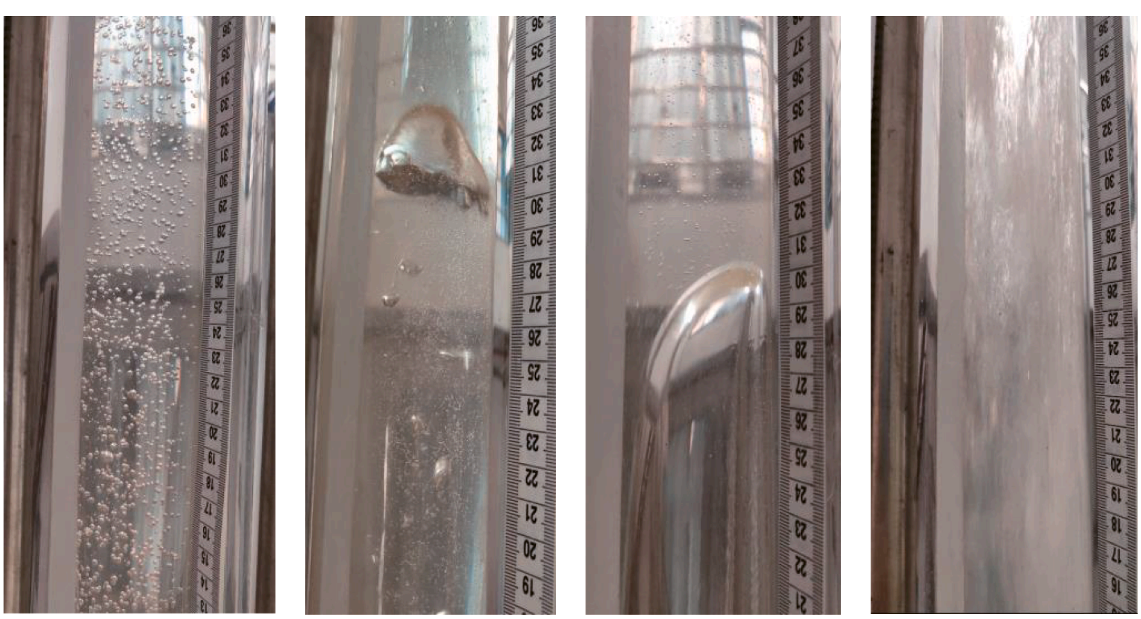

(a) Bubble flow **(b)** Cap-bubble flow **(c)** Slug flow **(d)** Annular flow

Fig. 2. Flow pattern in wellbore under gas–liquid counter-current flow.

(a) v_{sg} = 0.008 m·s^{-1} (b) v_{sg} = 0.06 m·s^{-1} (c) v_{sg} = 0.11 m·s^{-1}

Fig. 3. Variation of bubble flow with apparent gas velocity in gas–liquid counter-current flow (v_{sl} = 0.06 m·s^{-1}).

(a) v_{sl} = 0.05 m·s^{-1} (b) v_{sl} = 0.09 m·s^{-1} (c) v_{sl} = 0.13 m·s^{-1}

Fig. 4. Variation of bubble flow with apparent liquid velocity in gas–liquid counter-current flow (v_{sg} = 0.04 m·s^{-1}).

gas holdup under counter-current flow conditions, as represented in Eq. (1):

$$E_g = \frac{v_{sg}}{C_0(v_{sg} - v_{sl}) + v_d} \tag{1}$$

where E_g is the void fraction of cross section, dimensionless; v_{sg}, v_{sl} are the superficial gas velocity and the superficial liquid velocity, respectively, m/s; v_d is the bubble drift velocity, m/s; Under co-current two-phase flow conditions, the distribution coefficient C_0 is commonly assigned specific values based on the flow regime. For laminar flow conditions, C_0 is typically set to 2.0, while for turbulent flow conditions, a value of 1.2 is generally used. However, this study reveals that under gas–liquid counter-current flow conditions, the distribution coefficient differs significantly from that in co-current flow. Using the distribution coefficient derived from co-current conditions for calculations leads to deviations from actual conditions, resulting in substantial errors. To address this, we utilized the distribution coefficient model (2), which was developed in prior studies (Ren et al., 2024). Furthermore, we integrated the model (3) for cap-bubble rise velocity within a stationary liquid (Ren et al., 2024).

$$C_0 = 0.8 - 0.1\sin\theta \tag{2}$$

$$v_d = 1.53\left[\frac{g(\rho_l-\rho_g)\sigma}{\rho_l^2}\right]^{1/4}\left[1-0.052\ln\left(\frac{\mu_l}{\mu_w}\right)\right](1-E_g)^{0.85}\sqrt{\cos\theta} \tag{3}$$

where θ is the inclination angle of the wellbore, °; ρ_l and ρ_g are the densities of the liquid phase and gas phase, respectively, kg·m^{-3}; g is the gravitational acceleration, m·s^{-2}, taken as 9.81; μ_l and μ_w are the viscosities of the liquid phase and water, respectively, Pa·s; σ is the surface tension between the gas and liquid phases, N·m^{-1}.

The critical gas volume fraction is 0.15. Substituting Eqs. (2) and (3) into Eq. (1) yields the criterion for the transition from bubble flow to cap-bubble flow, as shown in Eq. (4). By substituting the apparent liquid phase velocity into Eq. (4), the critical velocity of the gas phase will be calculated, at which bubbly flow to cap-bubble flow transition occurs. When the liquid phase's apparent velocity within the pipe is substantial, the gas bubbles tend to migrate downward, which may result in the final term of Eq. (4) becoming negative. In this case, the gas and liquid both move downward. To tackle this issue, Eq. (4) is revised by incorporating the absolute value, leading to an updated model for the transition between flow regimes from bubbly flow to cap bubble flow in the context of gas–liquid counter-current flow, as illustrated in Eq. (5).

$$(1-C_0)v_{sg} = 0.15\left\{1.53\left[\frac{g(\rho_l-\rho_g)\sigma}{\rho_l^2}\right]^{1/4}\left[1 - 0.052\ln\left(\frac{\mu_l}{\mu_w}\right)\right](1-E_g)^{0.85}\sqrt{\cos\theta} - C_0 v_{sl}\right\} \tag{4}$$

$$(1-C_0)v_{sg} = 0.15\left|\left\{1.53\left[\frac{g(\rho_l-\rho_g)\sigma}{\rho_l^2}\right]^{1/4}\left[1 - 0.052\ln\left(\frac{\mu_l}{\mu_w}\right)\right](1-E_g)^{0.85}\sqrt{\cos\theta} - C_0 v_{sl}\right\}\right| \tag{5}$$

Bubble flow to cap bubble flow transition criterion under various experimental conditions was simulated using Eq. (5). The results obtained from the simulation were later contrasted with the relevant experimental data, as shown in Fig. 5.

As the apparent velocity of the liquid phase increases, the boundary that marks the transition between the different flow regimes adjusts accordingly. This shift occurs due to the reduced apparent velocity of the gas phase and the elevated apparent velocity of the liquid phase at this juncture, resulting in the gas bubbles being pushed backward while both phases continue to move downward. At the same time, as the liquid viscosity increases and the wellbore inclination angle increases, the bubble flow area decreases, and the conversion boundary will move towards a smaller liquid apparent velocity. This result is consistent with the experimental phenomenon. Increasing the viscosity of the liquid phase and the inclination of the wellbore will reduce the rising speed of small bubbles in the wellbore, and the bubbles are more likely to coalesce and form larger bubbles.

Therefore, the newly established bubble flow-cap bubble flow conversion boundary can accurately divide the bubble flow and the cap flow, and has a good response to the change of liquid viscosity and wellbore inclination.

2.2.2. *Cap bubble flow to slug flow transition*

Radovcich (1962) established that the critical gas volume fraction necessary for bubble coalescence and the transition to slug flow within the wellbore is 0.3. In a similar vein, Griffith and Wallis (1960) performed experiments that demonstrated a transition to slug flow when the gas volume fraction within the wellbore ranges from 0.25 to 0.3.

In this study, the relative motion between the gas and phases enhances the probability of gas bubbles merging within the wellbore. Analysis of the experimental results indicated that the minimum critical gas volume fraction is 0.25. Considering the influence of wellbore inclination, a wellbore correction factor is introduced for the critical gas volume fraction, as shown in Eq. (6). Furthermore, the previously established distribution coefficient model (Eq. (7)) and the Taylor bubble rise velocity model (Ren et al., 2024) in a static liquid phase (Eq. (8)) are employed in this analysis.

$$E_g = 0.25(1-\sin\theta)^{0.22} \tag{6}$$

$$C_0 = 0.658\cos^{0.658}\theta + 0.0219\left[\ln\left(\frac{\mu_l}{\mu_w}\right)\right]^{1.12} - 0.0108\left(\frac{v_{sl}}{v_{st}}\right)^{2.89} - 0.108 \tag{7}$$

$$v_d = (0.35\cos\theta + 0.45\sin\theta)\sqrt{\frac{gD(\rho_l-\rho_g)}{\rho_l}}\left[1-0.036\ln\left(\frac{\mu_l}{\mu_w}\right)\right] \tag{8}$$

The transition boundary of cap-bubble to slug flow is established by substituting Eqs. (6) and (8) into Eq. (1). This process yields the boundary described by Eq. (9).

$$\left(1-0.25(1-\sin\theta)^{0.22}C_0\right)v_{sg} = 0.25(1-\sin\theta)^{0.22}\times\left\{(0.35\cos\theta+0.45\sin\theta)\sqrt{\frac{gD(\rho_l-\rho_g)}{\rho_l}}\left[1-0.036\ln\left(\frac{\mu_l}{\mu_w}\right)\right]-C_0 v_{sl}\right\} \tag{9}$$

By inserting the apparent liquid phase velocity into Eq. (9), it is feasible to ascertain the critical apparent gas phase velocity required for the transition to slug flow at a given liquid velocity. In situations where the apparent liquid phase velocity in the wellbore is considerable, the gas bubbles are inclined to move downward, potentially resulting in the last term of Eq. (9) becoming

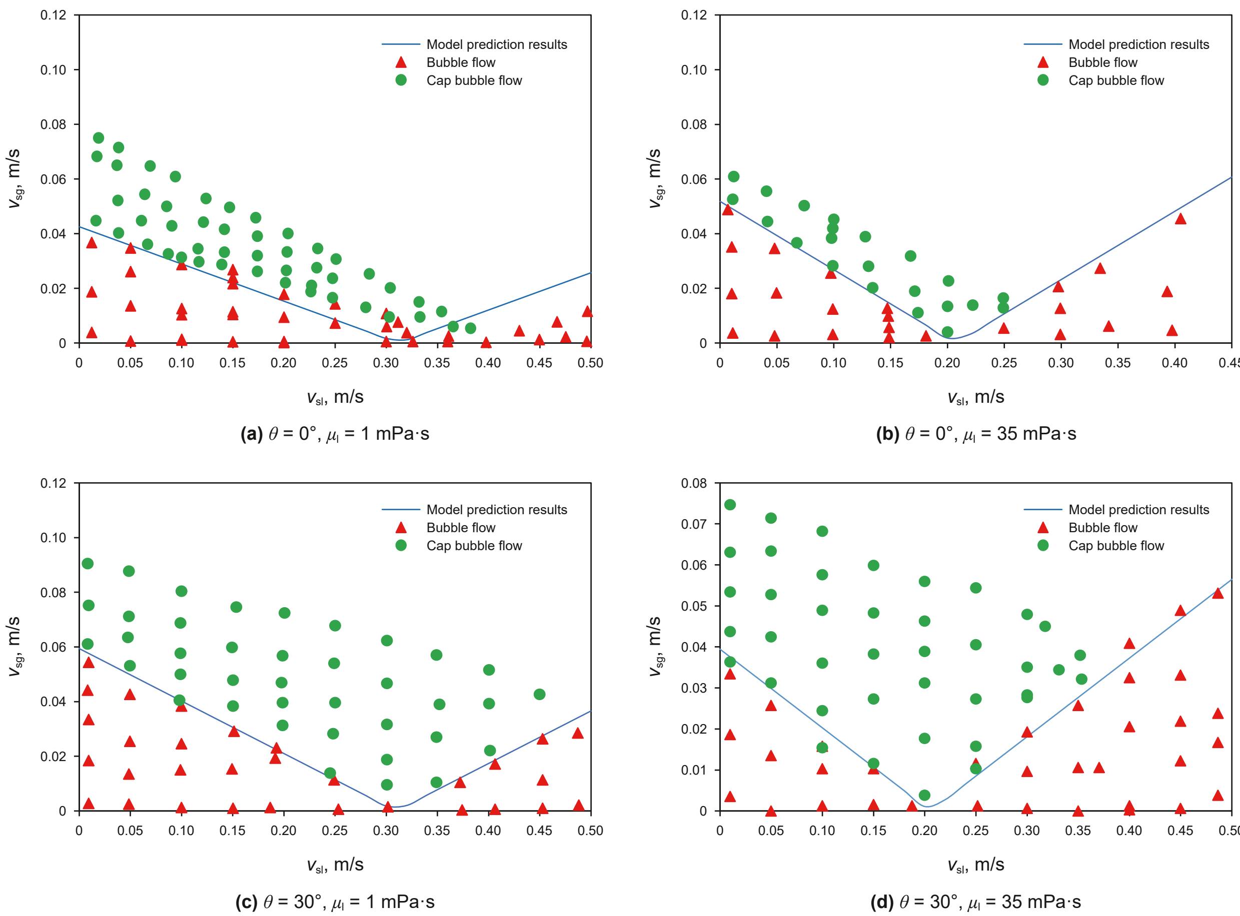

Fig. 5. Comparison between the experimental results and the prediction.

negative. To address this issue, an enhancement is introduced by applying the absolute value to the right side of Eq. (9). This adjustment results in the formulation of a gas–liquid counter-current flow model that describes the transition from cap bubble flow to slug flow, as illustrated in Eq. (10).

$$\left(1-0.25(1-\sin\theta)^{0.22}C_0\right)v_{sg}=0.25(1-\sin\theta)^{0.22}\times\left|\left\{(0.35\cos\theta+0.45\sin\theta)\sqrt{\frac{gD(\rho_l-\rho_g)}{\rho_l}}\left[1-0.036\ln\left(\frac{\mu_l}{\mu_w}\right)\right]-C_0v_{sl}\right\}\right| \quad (10)$$

The commonly used cap bubble-slug flow transition model under gas–liquid counter-current flow conditions is the one proposed by Taitel and Barnea (1983). Since Taitel and Barnea did not explicitly distinguish between the transitional flow regimes of cap bubble flow and slug flow, this study utilizes their defined boundary for the cap bubble-slug flow transition as the point of separation between these two types of flow. In their research, Taitel and Barnea proposed two criteria to define the transition from cap bubble flow to slug flow within the wellbore. The first criterion requires the resolution of a quadratic equation that takes into account the apparent gas velocity, apparent liquid velocity, and liquid hold-up. The second criterion stipulates that the gas volume fraction within the cross-section of the wellbore must remain below 0.3.

$$v_{sl}<v_{sg}+v_d-\sqrt{4v_{sg}v_d} \quad (11)$$

$$0.3v_{sl}+0.7v_{sg}<0.21v_d \quad (12)$$

In Eqs. (11) and (12), the model for bubble drift velocity is derived from the large bubble rise velocity framework introduced by Harmathy (1960). As depicted in Fig. 6, the transition boundary from cap bubble flow to slug flow, as forecasted by the model outlined in these equations, appears to be underestimated. The analysis indicates that this is due to the use of the distribution coefficient C_0 for co-current gas–liquid flow in Eqs. (11) and (12). The distribution coefficient for co-current flow exceeds that of counter-current flow, which causes the cap bubble-slug flow transition boundary to be underestimated.

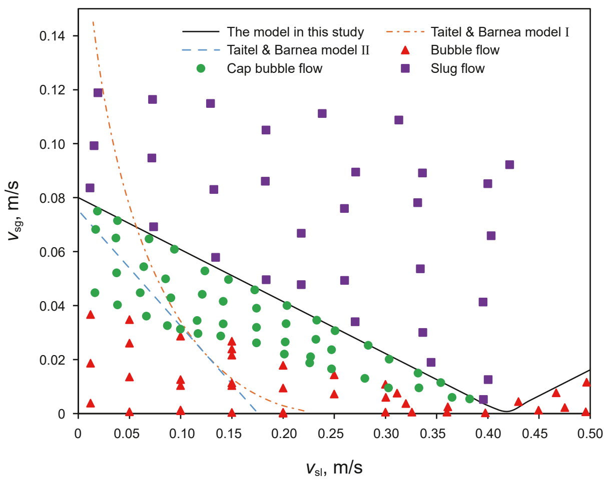

Fig. 6. Comparison of new model prediction and experimental results ($\theta = 30°$, $\mu_l = 35$ mPa·s).

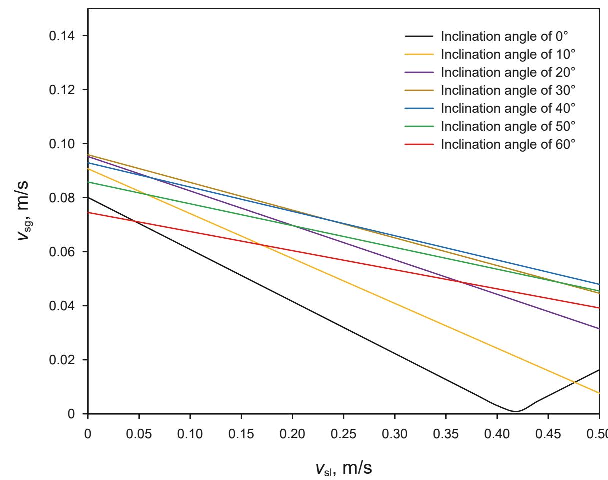

Fig. 8. Cap-bubble to slug flow pattern transition under different inclination angles (1 mPa·s).

As illustrated in Fig. 7, an increase in the viscosity of the liquid phase results in a downward shift of the transition boundary from cap bubble flow to slug flow. This alteration occurs because elevated liquid viscosity reduces the migration speed of gas bubbles. Consequently, this leads to a higher probability of bubble collisions, prompting them to merge into larger Taylor bubbles.

Showing in Fig. 8, as the inclination angle of the wellbore increases, cap-bubble to slug flow transition boundary initially rises, before gradually descending. Furthermore, as the inclination angle increases, no turning point is observed in the transition boundary. This is because, under the experimental conditions, the Taylor bubbles in the inclined wellbore cannot be easily pushed back. The increase in the inclination angle makes it more difficult to redirect and push the Taylor bubbles back into the wellbore.

From Figs. 6–8, it can be seen that the conversion criterion can accurately divide the flow pattern characteristics of gas–liquid reverse two-phase flow, and the response characteristics of liquid viscosity and wellbore inclination are consistent with the experimental phenomena, so it has good applicability.

2.2.3. Slug flow to annular flow transition

With a continued increase in the apparent gas phase velocity, the liquid slug within the slug unit becomes progressively unstable, eventually transforming into a continuous gas phase. This transformation gives rise to an annular flow pattern within the wellbore.

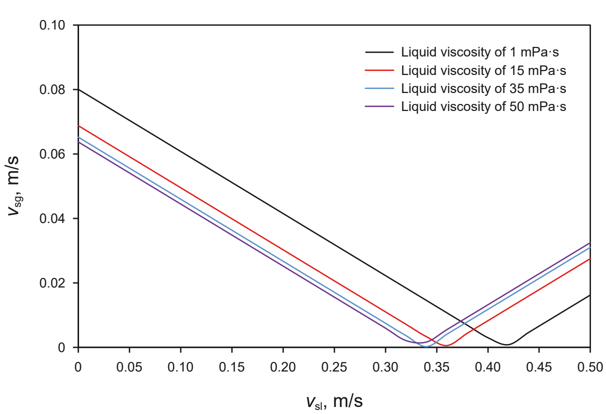

Fig. 7. Cap-bubble to slug flow pattern transition under different liquid viscosity ($\theta = 0°$).

When the gas-phase velocity increases to a certain extent, the downward flow of the liquid film is hindered, and liquid droplets are entrained into the gas core, causing the flow pattern in the wellbore to transition from slug flow to annular flow (McQuillan and Whalley, 1985; Jayanti and Hewitt, 1992). Wallis (1969) and Chen et al. (2015) studied the mechanisms of liquid entrainment in horizontal, vertical, and inclined wellbores through experiments and simulations. Among these, Wallis' critical velocity correlation is the most widely applied. In this research, the theory put forth by Wallis is applied, suggesting that when the liquid film surrounding the Taylor bubble experiences liquid entrainment, the flow pattern in the wellbore transitions from slug flow to annular flow.

By concentrating on the Taylor bubble as the central focus of this research, the flow rates for both the liquid and gas phases within the wellbore's cross-section can be calculated using Eqs. (13) and (14):

$$Q_f = \frac{4\delta}{D} A v_f \tag{13}$$

$$Q_s = \left(1 - \frac{4\delta}{D}\right) A v_{tb} \tag{14}$$

where δ represents the liquid film thickness, mm; v_f is the downward velocity of the liquid film, m·s^{-1}; v_{tb} is the upward velocity of the Taylor bubble, m·s^{-1}.

Utilizing the bubble migration velocity model previously developed (Ren et al., 2024), as indicated in Eq. (15), a continuity equation for the flow occurring within the wellbore is established, taking into account the direction of the fluid's movement. The resulting simplified equation is presented in Eq. (16).

$$v_{tb} = \left\{ 0.658 \cos^{0.658}\theta + 0.0219 \left[\ln\left(\frac{\mu_l}{\mu_w}\right) \right]^{1.12} - 0.0108 \left(\frac{v_{sl}}{v_{st}}\right)^{2.89} - 0.108 \right\} v_m + (0.35\cos\theta + 0.45\sin\theta) \sqrt{\frac{gD(\rho_l - \rho_g)}{\rho_l}} \left[1 - 0.036 \ln\left(\frac{\mu_l}{\mu_w}\right) \right] \tag{15}$$

$$v_{ss} - v_{fs} = v_{sg} - v_{sl} \tag{16}$$

where v_{ss} represents the superficial velocity of the Taylor bubble, $v_{ss} = Q_s/A$, $m \cdot s^{-1}$; v_{fs} represents the superficial velocity of the liquid film, $v_{fs} = Q_f/A$, $m \cdot s^{-1}$.

By incorporating Eqs. (13) and (14) into Eq. (16), a continuity equation related to the thickness and velocity of the liquid film is derived. The downward flow of the liquid film, along with the opposing movement of the gas–liquid phase, impacts the thickness of the liquid film, which is in turn affected by its superficial velocity. Consequently, the superficial velocity of the liquid film is expressed in Eq. (17):

$$v_{fs} = \frac{\mu_l}{4\rho_l D}\left\{\frac{\delta}{D}\frac{1}{B}\left[\frac{\mu_l^2}{D^3 g \rho_l(\rho_l - \rho_g)}\right]^{-p}\right\}^{1/q} \tag{17}$$

where B, p, and q are constants and dimensionless. Under laminar flow conditions, their values are 0.8667, 1/2, and 1/2, respectively. Under turbulent flow conditions, the values are 0.00448, 5/6, and 3/2. Wallis (1969) defined the liquid film Reynolds number, denoted as $Re_f = \rho_l v_{fs} \delta / \mu_l$. This parameter signifies that if the liquid film Reynolds number is less than 1000, the flow within the liquid film is classified as laminar. On the other hand, when the Reynolds number exceeds 1000, the flow shifts into a turbulent regime.

Wallis (1969) formulated a dimensionless correlation that relates the superficial gas velocity to the superficial liquid velocity, as presented in Eq. (18). Additionally, he identified the critical conditions necessary for liquid carryover to occur within the wellbore.

$$\left(J_g^*\right)^{1/2} + m\left(J_l^*\right)^{1/2} = C \tag{18}$$

where m and C are empirical constants, dimensionless; J_g^*, J_l^* represent the dimensionless superficial gas velocity, dimensionless superficial liquid velocity, respectively, and can be calculated using Eqs. (19) and (20).

$$J_g^* = v_{sg}\sqrt{\frac{\rho_g}{gD(\rho_l - \rho_g)}} \tag{19}$$

$$J_l^* = v_{sl}\sqrt{\frac{\rho_l}{gD(\rho_l - \rho_g)}} \tag{20}$$

This study employs the approach developed by McQuillan and Whalley (1985), replacing the superficial velocities of Taylor bubbles v_{ss} and the liquid film v_{fs} with the superficial gas velocity v_{sg} and the superficial liquid velocity v_{sl} in Eqs. (19) and (20). The upward velocity of the Taylor bubble is calculated using the bubble migration model presented in Eq. (15), which establishes the boundary for the transition from slug flow to annular flow, as shown in Eq. (21).

$$\left(v_{ss}^*\right)^{0.5} + m\left(v_{fs}^*\right)^{0.5} = C \tag{21}$$

In the equation, based on the findings of Wu et al. (2017), the values of m and C are taken as 0.85 and 1, respectively; v^*_{ss} and v^*_{fs} represent the dimensionless superficial velocity of the Taylor bubble and the dimensionless superficial velocity of the liquid film, which are calculated using Eqs. (22) and (23), respectively.

$$v_{ss}^* = v_{ss}\sqrt{\frac{\rho_g}{gD(\rho_l - \rho_g)}} \tag{22}$$

$$v_{fs}^* = v_{fs}\sqrt{\frac{\rho_l}{gD(\rho_l - \rho_g)}} \tag{23}$$

To summarize, the boundary that separates slug flow from annular flow is defined by Eqs. (21–23), in conjunction with the Taylor bubble migration model represented by Eq. (15), specifically under conditions of gas–liquid reverse flow. By assuming a specific value for the superficial liquid velocity (v_{sl}) and combining it with the Taylor bubble migration velocity model, it is possible to ascertain the critical superficial gas velocity necessary for the transition from slug flow to annular flow. This can be achieved by simultaneously solving Eqs. (21–23).

The slug to annular flow pattern transition was derived via simulation and subsequently validated against experimental findings, as depicted in Fig. 9.

The results indicate that the calculated outcomes of the model presented in this research align closely with the experimental observations. In contrast, the Wallis model (Wallis, 1969) and Taitel model (Taitel and Barnea, 1983) exhibit significant inaccuracies in identifying the transition boundary between slug flow and annular flow within the framework of gas–liquid reverse two-phase flow. This discrepancy can be attributed to the Wallis and Taitel models' dependence on a distribution coefficient model and the Taylor bubble migration velocity model that are intended for co-current gas–liquid flow, which tends to overestimate the transition boundary for this particular flow regime. In this research, modifications were made to both the distribution coefficient model and the Taylor bubble migration model tailored for gas–liquid reverse flow, so the prediction accuracy of the new model is higher under our data and Kim's data.

3. Two-phase flow model for bullheading well control method

To guarantee the safety of well control operations, it is crucial to continuously predict the wellbore pressure throughout the process. Therefore, for the bullheading well killing process, incorporating the bubble migration mechanism under gas–liquid counter-current flow and the flow pattern transition model, an unsteady gas–liquid two-phase counter-current flow model and its solution method have been established.

3.1. Basic equations

In the bullheading well control method, the continuity equation, momentum equation, and the overflow process in the two-phase flow within the wellbore exhibit comparable characteristics. However, auxiliary equations, such as the bubble migration velocity model and flow pattern transition model, along with boundary conditions, exhibit certain differences. To efficiently compute the well control parameters, this paper simplifies the model and makes the following assumptions.

(1) The drill string is concentric with the wellbore.
(2) Since the cross-sectional dimensions of the wellbore are much smaller than its longitudinal dimensions, for simplification, it is postulated that the fluid within the wellbore moves in a one-dimensional manner along the axis of the wellbore.
(3) The calculations consider only the movement of gas and liquid phases, focusing exclusively on their flow dynamics, with the assumption that there are no cuttings present within the wellbore.

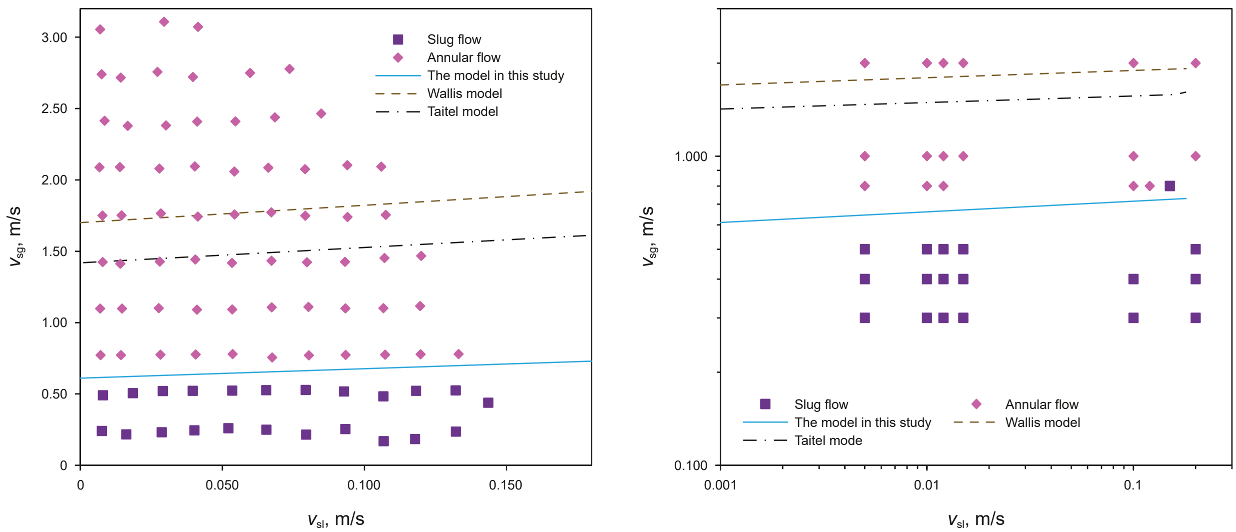

(a) This experiment, $\theta = 0°$ **(b)** Kim's experiment (Kim et al., 2001), $\theta = 0°$

Fig. 9. Comparison between predicted results and experimental results.

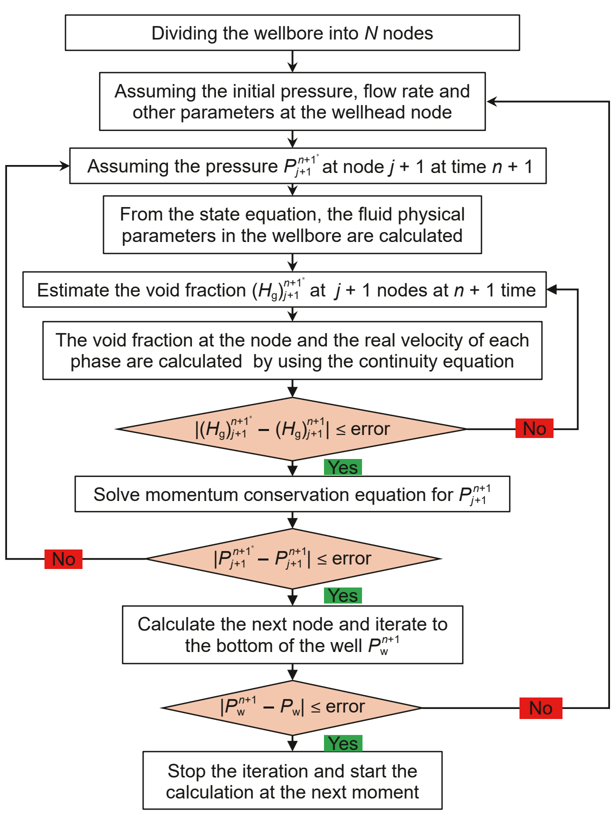

Fig. 10. Solving flow chart.

(4) It is presumed that the gas remains undissolved in the drilling fluid, and that no gas and liquid phase changes occur in wellbore.
(5) At a given point within the wellbore, liquid and gas exist with a thermodynamic equilibrium state, with no transfer of heat occurring between them.
(6) The well control fluid is assumed to be incompressible.

3.1.1. *Continuity equation*

(1) Continuity equation of gas phase.

Using the gas phase as a reference, let us examine a control volume situated within the flow path. By applying the principle of mass conservation, we can derive the following equation.

During gas kick,

$$\frac{\partial(AE_g\rho_g)}{\partial t}+\frac{\partial(AE_g\rho_g v_g)}{\partial s}=q_g \tag{24}$$

During well control,

$$\frac{\partial(AE_g\rho_g)}{\partial t}+\frac{\partial(AE_g\rho_g v_g)}{\partial s}=0 \tag{25}$$

(2) Liquid phase continuity equation

$$\frac{\partial(AE_l\rho_l)}{\partial t}+\frac{\partial(AE_l\rho_l v_l)}{\partial s}=q_l \tag{26}$$

where E_g and E_l represent the gas and liquid phase quality, dimensionless; A is the cross-sectional area of the flow path, m^2; v_g is the flow velocity of the gas phase, m·s^{-1}; v_l is the flow velocity of the liquid phase, m·s^{-1}; s is the spatial position, m; t is time, s.

3.1.2. *Momentum equation*

The equation governing the momentum in wellbore is formulated as follows:

$$\begin{aligned}&\frac{\partial}{\partial t}(AE_g\rho_g v_g+AE_l\rho_l v_l)+\frac{\partial}{\partial s}\left(AE_g\rho_g v_g^2+AE_l\rho_l v_l^2\right)\\&+Ag\cos\alpha(E_g\rho_g+E_l\rho_l)+A\frac{\mathrm{d}p}{\mathrm{d}s}+A\left|\frac{\mathrm{d}p}{\mathrm{d}s}\right|_{\mathrm{fr}}\\&=0\end{aligned} \tag{27}$$

where α is the wellbore inclination angle, °; p is the pressure term, Pa.

3.1.3. Auxiliary equation

In the process of well control using the bullheading well control method, the pressure loss consists of the frictional pressure drop of gas and liquid phase. The overall frictional pressure drop is represented by Eq. (28).

$$\left(\frac{\mathrm{d}p}{\mathrm{d}x}\right)_{\mathrm{f}}=\left(\frac{\mathrm{d}p}{\mathrm{d}x}\right)_{\mathrm{fl}}+\left(\frac{\mathrm{d}p}{\mathrm{d}x}\right)_{\mathrm{fg}} \tag{28}$$

(1) In the cases of bubble flow and cap-bubble flow, the velocity at which the gas phase is transported tends to be relatively low. As a result, when performing engineering calculations, the pressure drop related to the gas phase may be regarded as insignificant. Therefore, the total pressure drop under the conditions of bubble flow and cap-bubble flow can be expressed using Eq. (29).

$$\frac{\mathrm{d}p}{\mathrm{d}x}=-\rho_{\mathrm{m}}g+\frac{2}{D}f_{\mathrm{l}}\rho_{\mathrm{m}}v_{\mathrm{l}}^{2} \tag{29}$$

where f_{l} is the friction factor of liquid. The method for calculating frictional pressure drop differs across various flow regimes, as outlined in Eq. (30).

$$f_{\mathrm{l}}=\begin{cases}0.046\left(\dfrac{\rho_{\mathrm{l}}Dv_{\mathrm{l}}}{\mu_{\mathrm{l}}}\right)^{-0.2} & Re\leq 2000\\ f_{\mathrm{l}}(2000)+\dfrac{f_{\mathrm{l}}(3000)-f_{\mathrm{l}}(2000)}{1000}(Re-2000) & 2000<Re<3000\\ 16\left(\dfrac{\rho_{\mathrm{l}}Dv_{\mathrm{l}}}{\mu_{\mathrm{l}}}\right)^{-1} & Re\geq 3000\end{cases} \tag{30}$$

(2) In scenarios involving gas–liquid counter-current flow, the pressure drop linked to slug and annular flow primarily arises from the frictional pressure losses in both the gas and liquid phases. The method for calculating the frictional pressure drop is detailed below.

$$P_{j+1}^{n+1}-P_{j}^{n+1}=\frac{\Delta s}{2\Delta t}\left[\begin{array}{l}(E_{\mathrm{g}}\rho_{\mathrm{g}}v_{\mathrm{g}}+E_{1}\rho_{1}v_{1})_{j}^{n}+(E_{\mathrm{g}}\rho_{\mathrm{g}}v_{\mathrm{g}}+E_{1}\rho_{1}v_{1})_{j+1}^{n}\\-(E_{\mathrm{g}}\rho_{\mathrm{g}}v_{\mathrm{g}}+E_{1}\rho_{1}v_{1})_{j}^{n+1}-(E_{\mathrm{g}}\rho_{\mathrm{g}}v_{\mathrm{g}}+E_{1}\rho_{1}v_{1})_{j+1}^{n+1}\end{array}\right]+\left[\left(E_{\mathrm{g}}\rho_{\mathrm{g}}v_{\mathrm{g}}^{2}+E_{1}\rho_{1}v_{1}^{2}\right)_{j}^{n+1}-\left(E_{\mathrm{g}}\rho_{\mathrm{g}}v_{\mathrm{g}}^{2}+E_{1}\rho_{1}v_{1}^{2}\right)_{j+1}^{n+1}\right]$$
$$-\frac{\Delta s}{2}\left[(E_{\mathrm{g}}\rho_{\mathrm{g}}+E_{1}\rho_{1})_{j}^{n+1}+(E_{\mathrm{g}}\rho_{\mathrm{g}}+E_{1}\rho_{1})_{j+1}^{n+1}\right]-\frac{\Delta s}{2}\left\{\left[\left(\frac{\mathrm{d}p}{\mathrm{d}s}\right)_{\mathrm{fr}}\right]_{j}^{n+1}+\left[\left(\frac{\mathrm{d}p}{\mathrm{d}s}\right)_{\mathrm{fr}}\right]_{j+1}^{n+1}\right\} \tag{36}$$

In the context of slug flow and annular flow, the frictional pressure drop associated with the liquid phase can be expressed using Eq. (31).

$$\left(\frac{\mathrm{d}p}{\mathrm{d}x}\right)_{\mathrm{fl}}=\frac{2}{D}f_{\mathrm{l}}\rho_{\mathrm{l}}v_{\mathrm{l}}^{2} \tag{31}$$

The frictional pressure drop related to the gas phase in both slug flow and annular flow can be described by Eq. (32):

$$\left(\frac{\mathrm{d}p}{\mathrm{d}x}\right)_{\mathrm{fg}}=-\frac{2}{D-2\delta}f_{\mathrm{g}}\rho_{\mathrm{g}}\left(v_{\mathrm{g}}-v_{\mathrm{l}}\right)^{2} \tag{32}$$

where v_{l} is the real liquid velocity, m·s^{-1}; v_{g} is the real gas velocity, m·s^{-1}; f_{g} is the friction factor of gas, proposed by Chen (1979), as shown in Eq. (33):

$$\frac{1}{\sqrt{f}}=-2.0\log\left[\frac{\varepsilon}{3.7065D}-\frac{5.0452}{Re}\log\left(\frac{1}{2.8257}\left(\frac{\varepsilon}{D}\right)^{1.1098}+\frac{5.8506}{Re^{0.8981}}\right)\right] \tag{33}$$

where f is the frictional pressure drop, dimensionless; ε denotes the wellbore roughness, m; Re is the Reynolds number, dimensionless.

3.2. Discretization and solution of the equation

3.2.1. Discretization of the equation

Multiphase flow model was discretized based on the finite difference method, followed by the calculation of values at each location within the spatial domain. This process continues until all computations for every point in both the spatial and temporal domains are finalized. The specific difference forms are shown in Eqs. (34–36).

The continuity equation of gas,

$$(AE_{\mathrm{g}}\rho_{\mathrm{g}}v_{\mathrm{g}})_{j+1}^{n+1}-(AE_{\mathrm{g}}\rho_{\mathrm{g}}v_{\mathrm{g}})_{j}^{n+1}=\frac{\Delta s}{2\Delta t}\Big((AE_{\mathrm{g}}\rho_{\mathrm{g}})_{j}^{n}+(AE_{\mathrm{g}}\rho_{\mathrm{g}})_{j+1}^{n}-(AE_{\mathrm{g}}\rho_{\mathrm{g}})_{j}^{n+1}-(AE_{\mathrm{g}}\rho_{\mathrm{g}})_{j+1}^{n+1}\Big) \tag{34}$$

The continuity equation of liquid,

$$(AE_{1}\rho_{1}v_{1})_{j+1}^{n+1}-(AE_{1}\rho_{1}v_{1})_{j}^{n+1}=\frac{\Delta s}{2\Delta t}\Big((AE_{1}\rho_{1})_{j}^{n}+(AE_{1}\rho_{1})_{j+1}^{n}-(AE_{1}\rho_{1})_{j}^{n+1}-(AE_{1}\rho_{1})_{j+1}^{n+1}\Big) \tag{35}$$

The momentum equation,

3.2.2. Boundary conditions

Before performing the bullheading well control calculation, the state of each point in the wellbore can be obtained through a simulation of the overflow process. The aforementioned states serve as the starting conditions for the well control calculations.

Taking the initial conditions from the overflow process as an example.

$$v_g(s,0)=0 \tag{37}$$

$$E_g(s,0)=0 \tag{38}$$

$$P_a(s,0)=P(s) \tag{39}$$

$$v_{sl}(s,0)=\frac{Q_m}{\rho(s,0)A_a} \tag{40}$$

Throughout the bullheading process, the pressure at the bottom of the well is affected by several factors, including the formation pressure, the differential pressure resulting from formation flow, and the differential pressure due to losses. These flow and loss pressures require different calculation models depending on the formation characteristics, the layers can be categorized into two main types: permeable formations and fractured formations.

The calculation model for flow pressure differential differs when there is no mud cake and when mud cake is present. In the absence of mud cake, the flow pressure differential ΔP_L is calculated as follows (Zou et al., 2014):

$$\Delta P_L=\frac{3Q_f\mu}{2\pi Kh}\ln\frac{r_f}{r_w}+4\tau_0\left(r_f-r_w\right)\sqrt{\frac{\phi}{2K}} \tag{41}$$

where h is the lost zone thickness, m; Q_f is the lost circulation rate, $m^3\cdot s^{-1}$; r_f is the radius of the invasion zone, m; r_w is the wellbore radius, m; K is the formation permeability, μm^2; τ_0 is the yield point of the well control fluid, Pa; μ is the drilling fluid plastic viscosity, mPa·s; ϕ is the porosity, dimensionless.

When mud cake is present, the flow pressure differential is given:

$$\Delta P_L=\frac{Q_f}{2\pi h}\left(\frac{\mu_f}{K_m}\ln\frac{r_w}{r_m}+\frac{\mu_f}{K_n}\ln\frac{r_n}{r_w}\right) \tag{42}$$

where K_m is the permeability of the mud cake, μm^2; K_n is the permeability of the sealing layer, μm^2; μ_f is the killing fluid apparent viscosity, mPa·s; r_m is the radius of the wellbore with mud cake present, m; r_n is the radius of the sealing layer, m.

The pressure differential for lost circulation in fractured formations is as follows (Zou et al., 2014).

$$\Delta P_L=K\frac{h\mu^a\rho_l^{1-a}Q_f^{3-a}}{W^{a+1}}+\Delta P_0 \tag{43}$$

where K is an empirical coefficient, dimensionless; W denotes the fracture width, m; a is another empirical coefficient, dimensionless; ΔP_0 is the critical pressure differential for lost circulation, MPa.

During the well-control procedure, if we assume that the bottom hole pressure stays unchanged, it can be calculated by considering both the formation pressure and the differential pressure linked to the loss of circulation. After establishing the bottom hole pressure, this value can serve as a boundary condition for addressing the equations related to two-phase flow.

$$P(0,t)=\Delta P_L+P_e \tag{44}$$

3.2.3. The key parameter calculation methods for the bullheading well control method

(1) The density of killing fluid.

When planning the kill operation, selecting the correct density for the kill fluid is crucial. This choice must account for the formation pressure as well as the specific characteristics of the reservoir.

When the formation pressure is known, the appropriate density for the kill fluid can be calculated using the following method:

$$\rho_k=\frac{P_e}{gH}+\rho_s \tag{45}$$

where ρ_s is the additional equivalent density, typically ranging from 0.07 to 0.15 $g\cdot cm^{-3}$ for gas wells and 0.05–0.1 $g\cdot cm^{-3}$ for oil wells; ρ_k is the density of killing fluid, $g\cdot cm^{-3}$; P_e is the formation pressure, MPa; H is the well depth, m.

In cases where the formation pressure remains uncertain, the density of the kill fluid can be determined by utilizing existing data. This may include measurements such as the standing pipe pressure or the casing pressure noted after the well has been shut in.

Once the drill bit arrives at the well's bottom, the density of the kill fluid is established through the following method.

$$\rho_k=\frac{P_d+\rho_d gH}{gH}+\rho_s \tag{46}$$

When the drill bit is positioned away from the well's bottom, the density of the kill fluid is established through the following method:

$$\rho_k=\frac{P_d+\rho_d gh_d+\rho_m g(H-h_d)}{gH}+\rho_s \tag{47}$$

where ρ_d is the density of original drilling fluid, $g\cdot cm^{-3}$; ρ_m is the density of fluid from the drill bit to the well bottom, $g\cdot cm^{-3}$; P_d represents the standing pipe pressure, MPa; h_d is the length of the drill string inside the wellbore, m.

(2) The viscosity of killing fluid.

According to the previous research (Ren et al., 2024), with the increase of liquid viscosity, the rising velocity of bubbles in the wellbore decreases. Considering that the viscosity of the killing fluid commonly used in the field is 10–50 mPa·s, we recommends that the higher the viscosity of the killing fluid is, the better it is when the pump power and pressure bearing capacity are allowed.

(3) The well killing displacement.

After determining the density and viscosity of the killing fluid, the critical well killing displacement can be determined according to the degree of overflow, the bubble migration velocity model, and the flow pattern transformation model in Section 2.

The critical well-killing displacement associated with mild overflow pertains to a scenario in which the influx of gas is minimal. In this context, the kill fluid displacement required is only enough to redirect the small bubbles, ensuring successful well control. In practice, the actual killing displacement must be greater than the critical killing displacement. At the critical displacement, the migration speed of the small bubbles is zero, as given by Eq. (48).

$$v_g=1.0v_m+\frac{1}{18}\frac{\rho_l-\rho_g}{\mu_l}gd^2\left(1-E_g\right)^{-1.75}\sqrt{\cos\theta} \tag{48}$$

Therefore, the critical killing displacement is as follows:

$$Q_{cri}=\frac{\pi D^2}{4}\left[v_{sg}+\frac{1}{18}\frac{\rho_l-\rho_g}{\mu_l}gd^2\left(1-E_g\right)^{-1.75}\sqrt{\cos\theta}\right] \tag{49}$$

where D is the wellbore diameter, m; Q_c represents the critical kill fluid displacement, $m^3 \cdot s^{-1}$.

In cases of moderate overflow, most gas bubbles in the wellbore are cap-shaped bubbles. When the killing displacement equals the critical killing displacement, the migration velocity of the cap bubbles becomes zero, as given by Eq. (50).

$$v_g = (0.8 - 0.1\sin\theta)v_m + 1.53\left[\frac{g(\rho_l - \rho_g)\sigma}{\rho_l^2}\right]^{1/4}\left[1 - 0.052\ln\left(\frac{\mu_l}{\mu_w}\right)\right](1 - E_g)^{0.85}\sqrt{\cos\theta} \tag{50}$$

Therefore, the critical killing displacement is as follows.

$$Q_{cri} = \frac{\pi D^2}{4}\left\{\begin{array}{l}(0.8 - 0.1\sin\theta)v_{sg} + 1.53\left[\frac{g(\rho_l - \rho_g)\sigma}{\rho_l^2}\right]^{1/4} \times \\ \left[1 - 0.052\ln\left(\frac{\mu_l}{\mu_w}\right)\right](1 - E_g)^{0.85}\sqrt{\cos\theta}\end{array}\right\} \tag{51}$$

The critical kill fluid displacement associated with severe overflow pertains to a scenario characterized by a substantial gas inflow. The equation that defines the migration velocity of these Taylor bubbles can be found in Eq. (52).

$$v_g = \left(0.658\cos^{0.658}\theta + 0.0219\left[\ln\left(\frac{\mu_l}{\mu_w}\right)\right]^{1.12} - 0.0108\left(\frac{v_{sl}}{v_{st}}\right)^{2.89} - 0.108\right)v_m + (0.35\cos\theta + 0.45\sin\theta)\sqrt{\frac{gD(\rho_l - \rho_g)}{\rho_l}}\left[1 - 0.036\ln\left(\frac{\mu_l}{\mu_w}\right)\right] \tag{52}$$

Therefore, the critical killing displacement is as follows.

$$Q_{cri} = \frac{\pi D^2}{4}\left\{\begin{array}{l}\left(0.658\cos^{0.658}\theta + 0.0219\left[\ln\left(\frac{\mu_l}{\mu_w}\right)\right]^{1.12} - 0.0108\left(\frac{v_{sl}}{v_{st}}\right)^{2.89} - 0.108\right)v_{sg} + \\ (0.35\cos\theta + 0.45\sin\theta)\sqrt{\frac{gD(\rho_l - \rho_g)}{\rho_l}}\left[1 - 0.036\ln\left(\frac{\mu_l}{\mu_w}\right)\right]\end{array}\right\} \tag{53}$$

Various factors, including the pressure tolerance of the surface equipment, the fracture pressure at the casing shoe and the formation should be considered when designing the killing displacement. The killing displacement is given by Eq. (54).

$$Q_{cri} < Q < \min\{Q_1, Q_2, Q_3\} \tag{54}$$

where Q represents the killing displacement, m^3/s; Q_1 is the maximum killing displacement allowed by the pressure-bearing capacity of the surface equipment, m^3/s; Q_2 is the maximum killing displacement allowed by the fracture pressure of casing shoe, m^3/s; Q_3 is the maximum killing displacement allowed by the fracture pressure of wellbore bottom, m^3/s.

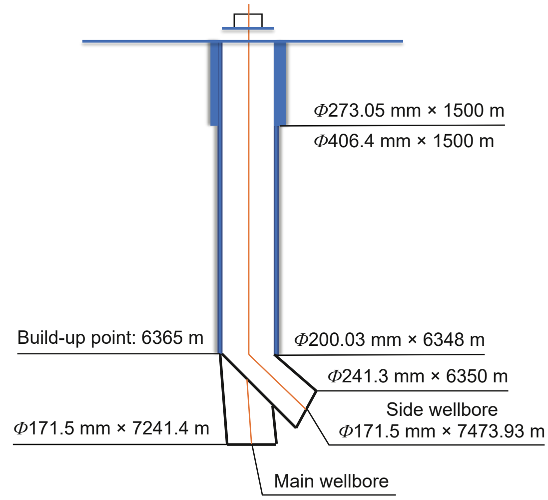

Fig. 11. Wellbore structure of the X1 well.

3.2.4. The process of solving

The model solving process and solving flow chart are as follows, shown in Fig. 10.

(1) First, determine parameters such as wellbore trajectory, casing structure, wellbore dimensions, and drill string configuration, then divide the wellbore into N nodes. This step serves as the foundation for the flow pattern analysis and modeling.
(2) Estimate initial parameters at the wellhead node, such as pressure and flow velocity. These initial conditions are crucial for identifying the starting flow pattern in the wellbore.
(3) Estimate the pressure at node j+1 at time n+1. This value will be compared with the calculated flow pattern to assess whether the flow is gas-dominant or liquid-dominant, as the flow pattern can influence pressure distribution.
(4) Using the equation of state, calculate the fluid properties within the wellbore. Characteristics like density and viscosity are vital in influencing the flow regime and the associated frictional losses, both of which are crucial for recognizing various flow patterns.
(5) Estimate the gas content at node j+1 at time n+1.
(6) Assess the characteristics of the fluids within the wellbore, along with the volume fractions. Then, input these into the continuity equation to calculate the velocity and gas content of the phases. At this point, an analysis of the flow pattern

should be performed. Flow pattern transition criteria must be utilized to assess the necessity of a transition in the flow pattern. The appropriate method for calculating frictional losses should be selected according to the identified flow pattern.

(7) If the error in the calculation falls within the defined tolerance limits, move on to the subsequent step. If not, revert to step 5 and recalculate until the conditions are met. If a flow pattern transition occurs during the recalculation, update the frictional loss calculation method accordingly.

(8) Using the momentum equation, calculate the pressure at time $n+1$ and node $j+1$, then compare it with the assumed pressure. If the difference between the two is smaller than the required error margin, it is considered correct, and the calculation continues. If a flow pattern transition is triggered, adjust the assumptions accordingly and return to step 3 for re-estimation of pressure at node $j+1$.

(9) Use the flow parameters at time $n+1$ and node $j+1$ as known conditions to calculate the next node. Ensure the selected flow pattern is still valid for the new conditions at each step.

(10) When performing iterative pressure calculations down to the well's bottom, it is essential to verify whether the outcomes satisfy the established boundary conditions. If they do, stop the iteration and begin the calculation for the next time step. If not, return to step 2 and adjust the wellhead pressure until the boundary conditions are satisfied.

In this combined approach, the key consideration is the integration of flow pattern identification with the iterative model solving process. This ensures that flow regime changes are accurately captured and that the corresponding changes in frictional losses, pressure distribution, and velocity profiles are incorporated into the model to enhance the accuracy of the simulation.

3.3. Model verification

The Tarim X1 well is classified as a directional well, and the configuration of its wellbore is illustrated in Fig. 11.

During drilling, at a depth of 7241.4 m, a blowout was encountered. After lifting the drilling string and shutting in the well, the casing pressure at the wellhead rose to 38 MPa within 0.5 min and eventually increased to 44 MPa. Based on geological conditions, it was predicted that the well contained high levels of hydrogen sulfide (H_2S). The maximum pressure rating of the blowout preventer (BOP) assembly is 70 MPa, and the conventional well control circulation method posed a high risk. Therefore, the bullheading well control method was prioritized for well control.

The well control measures implemented on-site utilized a kill fluid that had a density of 1.92 g·cm^{-3}. After injecting 155 m^3 of kill fluid into the annulus from the casing, the pump was stopped to wait and observe. At this stage, both the pressure of the wellhead casing and the drop in wellhead pressure were recorded at 0 MPa.

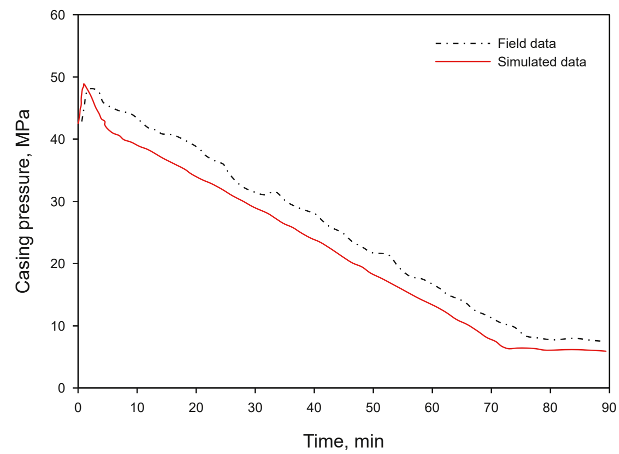

Fig. 12. Comparison between calculated results and measured values of well killing by bullheading method.

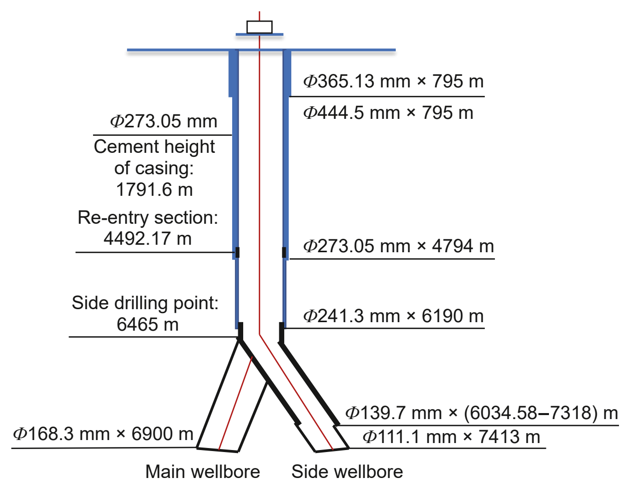

Fig. 13. Well structure of the X2 well.

Using the model proposed in this paper, a simulation calculation was performed for the X1 well conditions. Table 2 presents the assembly of the drilling string along with the associated engineering parameters.

As illustrated in Fig. 12, it was observed that the calculated casing pressure closely matched the field data. The discrepancy remained within a 15% margin. Initially, during the well-kill process, the formation leak-off pressure was larger than bottom hole pressure, while the wellhead casing pressure stood at 42.9 MPa. At

Table 2
Basic parameters of the X1 well.

Parameter	Value	Parameter	Value
Well depth	7241.4 m	Formation	Fractured-vuggy reservoir
Inner diameter of casing	200.03 mm	Formation pressure	72.5 MPa
Depth of casing	6367 m	Drilling fluid viscosity	30 mPa·s
Outer diameter of drill pipe (0–2480 m)	114.3 mm	Killing fluid viscosity	25 mPa·s
Outer diameter of drill pipe (2480–7241.4 m)	88.9 mm	Killing displacement	25 L·s^{-1}
Drilling fluid density	1.2 g·cm^{-3}	Thickness of loss zone	50 m
Killing fluid density	1.7 g·cm^{-3}	Average fracture width of the loss zone	0.2 mm
Surface temperature	25 °C	Diameter of drill bit	171.45 mm

Table 3
Basic parameters of X2 well.

Parameter	Value	Parameter	Value
Well depth	7418.84 m	Formation	Fractured-vuggy reservoir
Inner diameter of casing	200.03 mm	Formation pressure	156 MPa
Depth of casing	6190 m	Drilling fluid viscosity	30 mPa·s
Outer diameter of drill pipe (0–5184 m)	101.6 mm	Pit gain	4.6 m^3
Outer diameter of drill pipe (5184–6777 m)	73 mm	Diameter of drill bit	171.45 mm
Outer diameter of drill pipe (6777–7413 m)	80 mm	Depth of drill bit	7402.8 m
Surface tension	0.072 $N \cdot m^{-1}$	Deviation angle θ	0–6°

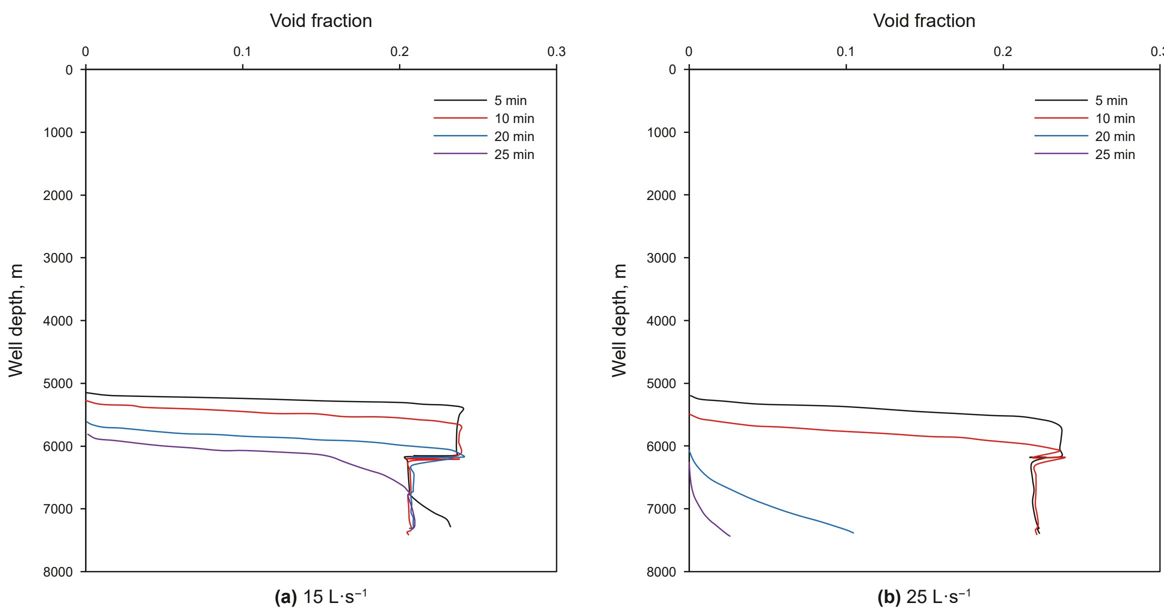

Fig. 14. Gas content changes in wellbore under different well killing displacement.

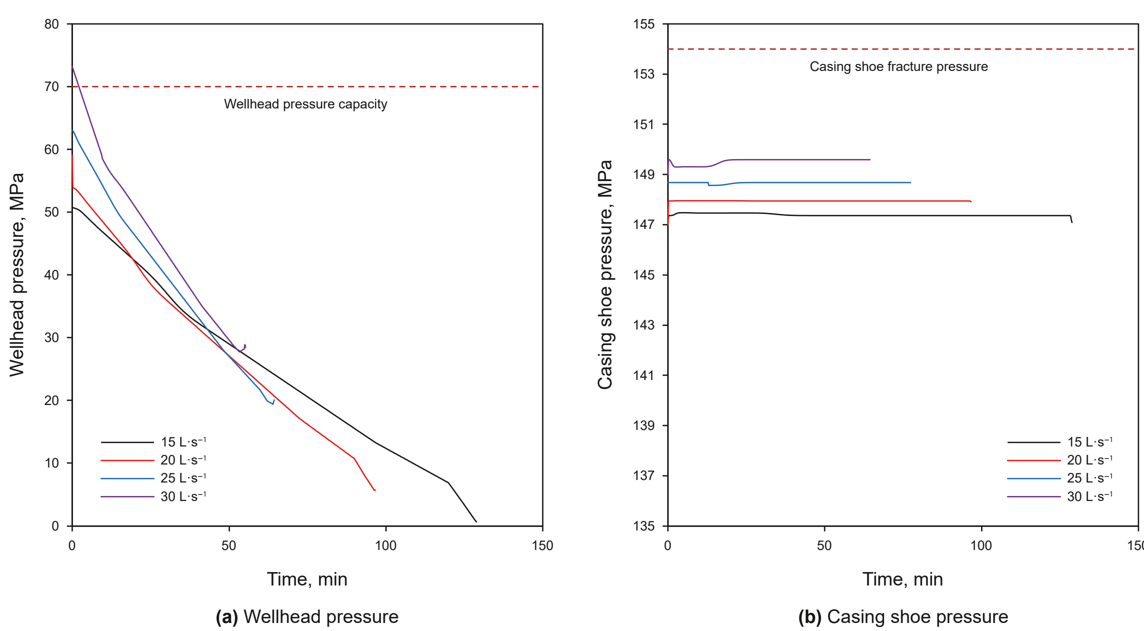

Fig. 15. Wellbore pressure change under different killing displacement.

this stage, kill fluid was pumped into well with 25 L·s^{-1}, which resulted in the compression of gas within the wellbore. The wellhead casing pressure increased rapidly. As the injection of kill fluid persisted, after a duration of 5 min, the formation fracture pressure was lower than bottom hole pressure. The gas was displaced to formation. Then, there was a gradual decline in the wellhead casing pressure. Following 72 min of effective well control, the influx gas was completely displaced to formation. The wellbore was filled with killing fluid. The wellhead casing pressure was stable, which indicated the successful completion of the kill operation utilizing the bullheading method for well control.

4. Results and analysis

Well killing parameters are the key to the success of well killing. In order to ensure the safety and efficiency of well killing operation, in addition to reasonably adjusting the well killing parameters, it is also necessary to consider the pressure bearing capacity of each part of the wellbore during the operation, and monitor the pressure change in the wellbore in real time. Based on the well structure of the X2 well (Fig. 13), through simulation analysis, the influence of different well killing parameters on well killing operation is explored, which lays a foundation for the optimization design of well killing parameters.

The X2 well, located in the Tarim Oilfield, is classified as a wildcat well, with a planned drilling depth set at 7650 m. The basic simulation parameters are shown in Table 3.

4.1. The influence of killing displacement

A viscosity of 30 mPa·s has been selected for the killing fluid. Taking into account the formation pressure, the killing fluid density has been determined to be 2.12 g·cm^{-3} according to Eq. (45). By utilizing the parameters of the wellbore structure, the drill string, and the characteristics of the kill fluid, the calculated critical flow rate for the well-killing operation is found to be 13.6 L·s^{-1}. A series of simulations were performed to analyze the well-killing process at various flow rates, leading to the generation of pressure distribution profiles within the wellbore corresponding to different well-killing parameters, as illustrated in Figs. 14 and 15.

Fig. 14 illustrates that a rise in the flow rate of the well-killing fluid leads to a notable decrease in the duration required for well-killing operations. When flow velocity is 15 L·s^{-1}, following 25 min of well-killing, the gas front in the wellbore is positioned at 5885.2 m. In contrast, when the flow rate increases to 25 L·s^{-1}, after the same duration of 25 min, the gas front moves to a depth of 6802.9 m, where the gas content near the bottom is significantly lower, and most of the gas has already been returned to the formation.

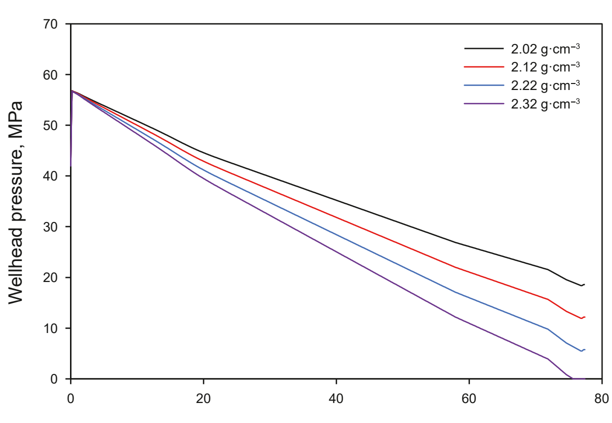

Fig. 16. Wellhead pressure changes when killing fluid density is different.

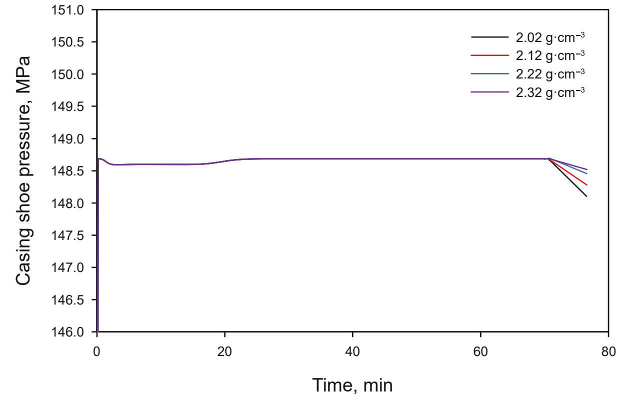

Fig. 17. Casing shoe pressure variation when killing fluid density is different.

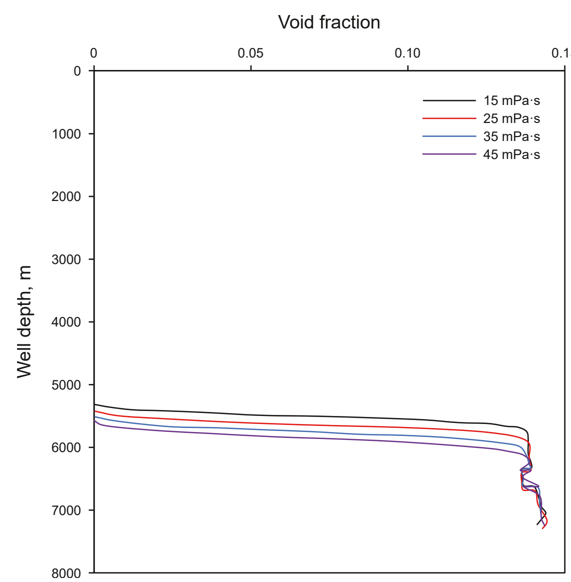

Fig. 18. Gas content changes in wellbore under different killing fluid viscosity.

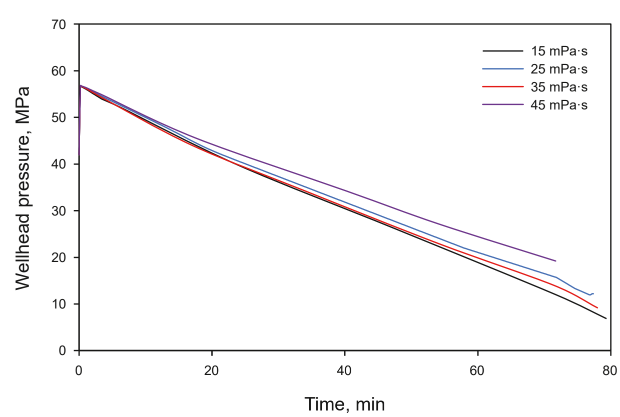

Fig. 19. Wellhead pressure changes under different killing fluid viscosity.

However, it can be seen from Fig. 15 that the larger the well killing displacement, the greater the wellhead back pressure and the pressure at the casing shoe during the well killing process, and there is a higher risk of well killing operation. When the kill rate is 30 L·s^{-1}, the initial wellhead pressure is 73.2 MPa, which exceeds the wellhead's pressure tolerance.

Therefore, in the process of well killing by pressure back method, under the premise of ensuring safe construction, a larger well killing displacement can be selected for operation, so as to ensure the efficient operation of well killing. Subsequently, well killing simulation is carried out at 25 L·s^{-1}.

4.2. The effect of killing fluid density

The bullheading operation is performed when the flow velocity is 25 L·s^{-1} and well-killing fluid viscosity is 25 mPa·s. The well-killing fluids have densities of 2.02, 2.12, 2.22 and 2.32 g·cm^{-3}, with the simulation results presented in Figs. 16 and 17.

As illustrated in Figs. 16 and 17, at the onset of the well-killing procedure, the initial pressure at the wellhead remains nearly identical when various densities of well-killing fluids are employed. Additionally, the pressure observed at the casing shoe exhibits only minor differences, indicating minimal variation despite the changes in fluid density.

With the increase of killing time, the greater the density of killing fluid, the smaller the wellhead pressure, and the completion time of killing operation is basically the same. For the pressure at the casing shoe, when the killing fluid reaches the casing shoe, the pressure at the casing shoe gradually decreases due to the constant bottom hole pressure, and the greater the density of the killing fluid, the faster the pressure at the casing shoe decreases. This is obviously different from the cyclic killing. In the process of cyclic killing, the greater the density of the killing fluid, the greater the pressure at the casing shoe.

Consequently, by deliberately enhancing the density of the well-killing fluid, one can efficiently lower both the wellhead pressure and the casing shoe pressure throughout the operation.

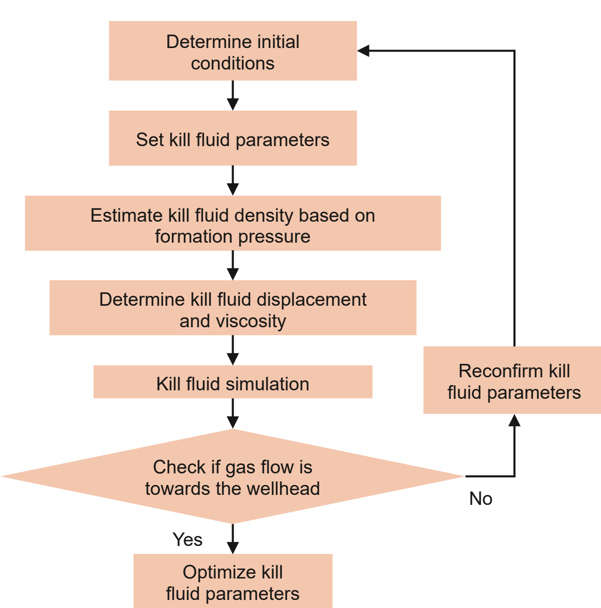

Fig. 20. Killing parameter optimization process.

Table 4
Well killing parameter calculation results of the X2 well.

Well killing parameters	Value				
Density of killing fluid, g·cm^{-3}	2.12	2.12	2.12	2.12	2.12
Viscosity of killing fluid, mPa·s	25	25	25	25	25
Killing displacement, L·s^{-1}	10	15	20	25	30
Well control time, min	Fail	147.1	96.4	77.4	64.4
Maximum pressure at well head, MPa	—	50.8	54.5	63	73.2
Pressure at casing shoe, MPa	—	147.4	147.9	148.7	149.6
Maximum bottom hole pressure, MPa	—	150.8	151.9	152.7	153.9

4.3. The influence of killing fluid viscosity

A killing simulation was conducted using a killing fluid with a flow rate of 25 L·s^{-1} and a density of 2.12 g·cm^{-3}, with viscosities ranging from 15 to 45 mPa·s. The results of the simulation are presented in Figs. 18 and 19.

Fig. 18 demonstrates that, under constant well-killing time and flow rate, an increase in fluid viscosity causes the gas front position to move closer to well bottom. This effect arises from the fact that increased viscosity slows down the upward movement of gas within the wellbore, which ultimately results in a longer duration for the well-killing operation.

However, as shown in Fig. 19, a higher viscosity of the killing fluid leads to greater casing pressure at the wellhead during the well-killing process, resulting in relatively high wellhead pressure upon completion. Therefore, to balance both killing efficiency and wellhead pressure, field operations can initially use high-viscosity kill fluid to decelerate and suppress the influx gas through bullheading, followed by switching to low-viscosity kill fluid to ultimately bring the wellhead pressure back to 0 MPa.

4.4. The key well control parameters optimization

From the above simulation results, it can be seen that the flow rate, the density and the viscosity of killing fluid affect the wellhead pump pressure, the pressure at the casing shoe and the killing time, among which the flow rate has the most significant influence. The density and viscosity of killing fluid have little effect on the initial wellhead casing pressure and casing shoe pressure. Therefore, the optimal design of well killing should first consider the displacement of well killing fluid. The density of killing fluid is obtained by formation pressure. The viscosity of killing fluid is commonly used in the site within 10–50 mPa·s. The higher the viscosity of killing fluid, the more conducive to the efficient construction of killing well. Before executing well-killing procedures, this model can be employed to simulate and evaluate the complete process, aiding in the determination of the most efficient strategy for well-killing. The procedure for optimizing the well-killing design is illustrated in Fig. 20.

In this study, the X2 well is used as a case example, where the fluid density is selected as 2.12 g·cm^{-3} and the fluid viscosity is 25 mPa·s. Impact of varying killing fluid displacement on the construction parameters for the X2 well is computed, as presented in Table 4. The wellhead will be overpressure when flow velocity is 30 L·s^{-1}. Consequently, fluid flow velocity should be kept within the range of 15–25 L·s^{-1}. Within this specified range, using a fluid viscosity of 25 mPa·s and a density of 2.12 g·cm^{-3}, no overpressure is observed at either the wellhead or the bottom of the well. Therefore, the proposed well-killing strategy is deemed feasible.

5. Conclusions

Based on the flow pattern transition criteria for gas–liquid counter-current two-phase flow, a multiphase flow model for bullheading operations was developed. The simulation results reveal the variation patterns of multiphase flow parameters in the wellbore during bullheading, and furthermore, an optimal design methodology for bullheading parameters is proposed.

(1) The increase of wellbore inclination angle and liquid viscosity promotes the transformation of bubbly flow-slug flow. The prediction accuracy of the newly established flow pattern transformation model is better than that of Taitel-Barnea and Wallis models.
(2) During bullheading operations, the counter-current gas–liquid two-phase flow model can effectively calculate the variations in multiphase flow parameters within the wellbore. Comparison with the measured casing pressure data from Well X1 at different stages shows that the error margin is within 15%.
(3) The killing displacement has a great influence on the construction parameters. The larger the killing displacement is, the shorter the killing time is, but the greater the wellhead casing pressure is. Conversely, the higher the density of killing fluid is, the smaller the wellhead casing pressure drop is. The viscosity of killing fluid has the least influence. Within the limits of equipment safety and formation bearing capacity, high-displacement, high-viscosity kill operations can be considered initially, followed by a gradual reduction in displacement rate and viscosity.

In the future, further research should be carried out in the following aspects: The killing parameters in this study are based on laboratory tests, and field experiments can be carried out in subsequent studies to improve the accuracy of the model. Secondly, the bubble migration behavior in the gas–liquid-solid three-phase can be studied in combination with the field conditions, so that the calculation results are closer to the field conditions.

CRediT authorship contribution statement

Bang-Tang Yin: Writing – review & editing, Writing – original draft, Validation, Supervision, Investigation, Formal analysis, Conceptualization. **Tian-Bao Ding:** Writing – original draft, Validation, Methodology, Formal analysis. **Wei Zhang:** Validation, Methodology. **Shu-Long Wang:** Formal analysis. **Zhi-Yuan Wang:** Supervision, Methodology. **Bao-Jiang Sun:** Writing – original draft, Methodology. **Xu-Liang Zhang:** Methodology. **Qian-Li Ma:** Writing – review & editing, Methodology.

Declaration of competing interest

The authors declare that they have no known competing financial interests or personal relationships that could have appeared to influence the work reported in this paper.

Acknowledgement

This paper was sponsored by National Natural Science Foundation of China (52288101, 52274020), the Fund of State Key Laboratory of Deep Oil and Gas, China University of Petroleum (East China) (No. SKLDOG2025-SDRC-02).

References

Besagni, G., Inzoli, F., 2016. Comprehensive experimental investigation of counter-current bubble column hydrodynamics: Holdup, flow regime transition, bubble size distributions and local flow properties. Chem. Eng. Sci. 146, 259–290. https://doi.org/10.1016/j.ces.2016.02.043.
Burchette, T.P., 2012. Carbonate rocks and petroleum reservoirs: a geological perspective from the industry. Geol. Soc. Lond. Spec. Publ. 370 (1), 17–37. https://doi.org/10.1144/sp370.14.
Chen, J., Tang, Y., Zhang, W., et al., 2015. Computational fluid dynamic simulations on liquid film behaviors at flooding in an inclined pipe. Chin. J. Chem. Eng. 23 (9), 1460–1468. https://doi.org/10.1016/j.cjche.2015.07.012.
Chen, N.H., 1979. An explicit equation for friction factor in pipe. Ind. Eng. Chem. Fundam. 18 (3), 296–297. https://doi.org/10.1021/i160071a019.
Flores-Avila, F.S., Smith, J.R., Bourgoyne Jr, A.T., et al., 2002. Experimental evaluation of control fluid fallback during off-bottom well control: Effect of deviation angle. In: IADC/SPE Drilling Conference. https://doi.org/10.2118/74568-MS.
Flores-Avila, F.S., Smith, J.R., Bourgoyne, Jr, A.T., 2003. New dynamic kill procedure for off-bottom blowout wells considering counter-current flow of kill fluid. In: SPE/IADC Middle East Drilling Technology Conference and Exhibition. https://doi.org/10.2118/85292-MS.
Ghiaasiaan, S.M., Taylor, K.E., Kamboj, B.K., et al., 1995. Countercurrent two-phase flow regimes and void fraction in vertical and inclined channels. Nucl. Sci. Eng. 119 (3), 182–194. https://doi.org/10.13182/NSE95-A24084.
Ghiaasiaan, S.M., Wu, X., Sadowski, D.L., et al., 1997. Hydrodynamic characteristics of counter-current two-phase flow in vertical and inclined channels: Effects of liquid properties. Int. J. Multiphas. Flow 23 (6), 1063–1083. https://doi.org/10.1016/S0301-9322(97)00027-X.
Ghosh, S., Pratihar, D.K., Maiti, B., et al., 2012. Identification of flow regimes using conductivity probe signals and neural networks for counter-current gas-liquid two-phase flow. Chem. Eng. Sci. 84, 417–436. https://doi.org/10.1016/j.ces.2012.08.042.
Griffith, P., Wallis, G.B., 1960. Two-phase slug flow. J. Heat Tran. 83 (3), 307–318. https://doi.org/10.1115/1.3682268.
Harmathy, T.Z., 1960. Velocity of large drops and bubbles in media of infinite or restricted extent. Am. Inst. Chem. Eng. J. 6 (2), 281–288. https://doi.org/10.1002/aic.690060222.
Hasan, A.R., Kabir, C.S., Srinivasan, S., 1994. Countercurrent bubble and slug flows in a vertical system. Chem. Eng. Sci. 49 (16), 2567–2574. https://doi.org/10.1016/0009-2509(94)E0084-4.
Jayanti, S., Hewitt, G.F., 1992. Prediction of the slug-to-churn flow transition in vertical two-phase flow. Int. J. Multiphas. Flow 18 (6), 847–860. https://doi.org/10.1016/0301-9322(92)90063-M.
Kim, H.Y., Koyama, S., Matsumoto, W., 2001. Flow pattern and flow characteristics for counter-current two-phase flow in a vertical round tube with wire-coil inserts. Int. J. Multiphas. Flow 27 (12), 2063–2081. https://doi.org/10.1016/S0301-9322(01)00052-0.
Liu, H., Liu, H., Zhang, Q., et al., 2023. Effect of liquid viscosity on the gas-liquid two phase countercurrent flow in the wellbore of bullheading killing. Geoenergy Sci. Eng. 221, 111274. https://doi.org/10.1016/j.petrol.2022.111274.
McQuillan, K.W., Whalley, P.B., 1985. Flow patterns in vertical two-phase flow. Int. J. Multiphas. Flow 11 (2), 161–175. https://doi.org/10.1016/0301-9322(85)90043-6.
Mu, L., Chen, Y., Xu, A., et al., 2020. Technological progress and development directions of PetroChina overseas oil and gas exploration. Petrol. Explor. Dev. 47 (1), 1088–1099. https://doi.org/10.1016/S1876-3804(20)60011-8.
Oudeman, P., 1999. Kill procedures to avoid formation damage in the high rate gas wells of an underground storage project. In: SPE European Formation Damage Conference and Exhibition. https://doi.org/10.2118/54761-MS.
Oudeman, P., ter Avest, D., Grodal, E.O., et al., 1994. Bull heading to kill live gas wells. In: European Petroleum Conference. https://doi.org/10.2118/28896-MS.
Pal, S., Mushtaq, M., Banat, F., et al., 2018. Review of surfactant-assisted chemical enhanced oil recovery for carbonate reservoirs: Challenges and future perspectives. Pet. Sci. 15, 77–102. https://doi.org/10.1007/s12182-017-0198-6.
Radovcich, N.A., 1962. The Transition from Two Phase Bubble Flow to Slug Flow. Massachusetts Institute of Technology. http://hdl.handle.net/1721.1/61460.
Ren, M., Ding, T., Yin, Z., et al., 2024. Migration characteristics of bubbles moving in gas–liquid countercurrent two-phase flow in an inclined pipe. Phys. Fluids 36, 093322. https://doi.org/10.1063/5.0226376.
Sukamta, S., Firdaus, R.A., Thoharudin, T., 2018. The characteristic of two-phase flow pattern on air-water countercurrent flow in vertical pipe. Key Eng. Mater. 792, 190–194. https://doi.org/10.4028/www.scientific.net/KEM.792.190.
Taitel, Y., Barnea, D., 1983. Counter current gas-liquid vertical flow, model for flow pattern and pressure drop. Int. J. Multiphas. Flow 9 (6), 637–647. https://doi.org/10.1016/0301-9322(83)90113-1.
Tan, Y., Li, Q., Xu, L., et al., 2022. A critical review of carbon dioxide enhanced oil recovery in carbonate reservoirs. Fuel 328, 125256. https://doi.org/10.1016/j.fuel.2022.125256.
Teng, X., Sun, B., Zhang, Y., et al., 2018. A five-step bullheading killing well control method for fractured formations without a safety pressure window. Petrol. Drill. Tech. 46 (6), 20–25. https://doi.org/10.11911/syztjs.2018157 (in Chinese).
Wallis, G.B., 1969. One-Dimensional Two-phase Flow. McGraw-Hill, New York.
Wang, X., Liu, H., Zhao, M., et al., 2025. Study on multiphase flow modeling and parameter optimization design for bullheading. Geoenergy Sci. Eng. 245, 213519. https://doi.org/10.1016/j.geoen.2024.213519.
Wu, B., Firouzi, M., Mitchell, T., et al., 2017. A critical review of flow maps for gas-liquid flows in vertical pipes and annuli. Chem. Eng. J. 326, 350–377. https://doi.org/10.1016/j.cej.2017.05.135.
Yamaguchi, K., Yamazaki, Y., 1982. Characteristics of counter current gas-liquid two-phase flow in vertical tubes. J. Nucl. Sci. Technol. 19 (12), 985–996. https://doi.org/10.1080/18811248.1982.9734247.

Yamaguchi, K., Yamazaki, Y., 1984. Combinated flow pattern map for cocurrent and countercurrent air-water flows in vertical tube. J. Nucl. Sci. Technol. 21 (5), 321–327. https://doi.org/10.1080/18811248.1984.9731053.

Zhou, Y., Li, Q., Liu, S., 2021. Influence on bottom hole pressure during killing process of gas wells using bullheading method considering gas-liquid replacement. J. Saf. Sci. Tech. 17 (3), 103–109. https://doi.org/10.11731/j.issn.1673-193x.2021.03.016 (in Chinese).

Zou, D., Zhao, J., Guo, Y., et al., 2014. A model for predicting leak off pressure in permeable sandstone formations. Petrol. Drill. Tech. 42 (1), 33–36. https://doi.org/10.3969/j.issn.1001-0890.2014.01.006 (in Chinese).